# High entropy fluorides as conversion cathodes with tailorable electrochemical performance

Yanyan Cui [a,1], Parvathy Anitha Sukkurji [a,1], Kai Wang [a], Raheleh Azmi [b], Alexandra M. Nunn [a,c], Horst Hahn [a,d], Ben Breitung [a], Yin-Ying Ting [e], Piotr M. Kowalski [e], Payam Kaghazchi [f], Qingsong Wang [a,*], Simon Schweidler [a,*], Miriam Botros [a,*]

[a] Institute of Nanotechnology, Karlsruhe Institute of Technology (KIT), Hermann-von-Helmholtz-Platz 1, 76344 Eggenstein-Leopoldshafen, Germany
[b] Institute for Applied Materials–Energy Storage Systems, Karlsruhe Institute of Technology (KIT), Hermann-von-Helmholtz-Platz 1, 76344 Eggenstein-Leopoldshafen, Germany
[c] Faculty of Science, University of Waterloo, Waterloo, ON N2L 3G1, Canada
[d] KIT-TUD-Joint Research Laboratory Nanomaterials, Technical University Darmstadt, Darmstadt 64287, Germany
[e] Theory and Computation of Energy Materials (IEK-13), Institute of Energy and Climate Research, Forschungszentrum Jülich GmbH, 52425 Jülich, Germany
[f] Materials Synthesis and Processing (IEK-1), Institute of Energy and Climate Research, Forschungszentrum Jülich GmbH, 52425 Jülich, Germany

*Keywords:*
High entropy materials
High entropy fluorides
Conversion cathodes
Tailored electrochemistry
Li-ion batteries

A B S T R A C T

With the recent development of high entropy materials, an alternative approach to develop advanced functional materials with distinctive properties that show improved values compared to conventional materials has been provided. The high entropy concept was later successfully transferred to metal fluorides and high entropy fluorides (HEFs) were successfully synthesized. Owing to their high theoretical specific capacities in energy storage applications, HEFs were utilized as cathode materials for lithium-ion batteries (LIBs) and their underlying storage mechanisms were investigated. Instead of a step-by-step reduction of each individual metal cation, the HEFs seem to exhibit a single-step reduction process, indicating a solid solution compound instead of merely a mixture of different metal fluorides. It was also observed that the electrochemical behavior of the HEFs depends on each individual incorporated element. Therefore, by altering the elemental composition, new materials that exhibit improved electrochemical properties can be designed. Remarkably, HEFs with seven incorporated metal elements exhibited a better cycling stability as well as a lower hysteresis compared to binary metal fluorides. These findings offer new guidelines for material design and tailoring towards high performance LIBs.

## 1. Introduction

With rapidly increasing demands for portable electronics and electric vehicles, the development of secondary lithium-ion batteries (LIBs) with high energy densities is necessary. In current LIB technology, the cell voltage and capacity are largely determined by the cathode material, which also dominates the battery cost. Therefore, it is important to explore alternative cathode materials and to investigate their structure/composition/performance relationships for further development [1]. As an example, conversion-based electrode materials, which serve a potentially higher specific capacity than conventional intercalation-based electrode materials, have drawn great attention in recent years [2]. Since in a conversion reaction, multiple electrons ($n \geq 2$) can be transferred per formula unit during the redox reaction, conversion materials can deliver capacities three to five times larger compared to intercalation materials [3]. Among the different conversion material types, metal fluorides (MFs) show a relatively high lithiation potential due to the large enthalpy of formations [4–6]. Additionally, MFs show high volumetric and gravimetric capacities, which enable them to be attractive candidates for high energy density cathode materials [7,8].

Unfortunately, conversion materials suffer from large volume changes upon cycling and unfavorable interactions between the active material and the electrolyte [9]. The former can lead to cracking of individual particles, structural disintegration, swelling of the electrode, and disconnection of the active material. The latter is accompanied by a loss of active material, re-precipitation of cathode components which can lead to blockage of the ion path-

* Corresponding authors.
*E-mail addresses:* qingsong.wang@kit.edu (Q. Wang), simon.schweidler@kit.edu (S. Schweidler), miriam.botros@kit.edu (M. Botros).
[1] These authors contributed equally to this work.

ways, and migration of soluble species to the anode side which negatively affects the SEI (blockage of the anode) [10,11]. In addition, electrolyte decomposition can also occur (gas evolution), which is a relevant factor from a safety point of view. Overall, these interrelated processes may lead to an increase in cell resistance, poor cycling performance, and poor Coulombic efficiency [2,12,13]. In order to circumvent these issues and to realize the application of MFs in rechargeable batteries, cation or anion doping is an important strategy to improve the electrochemical properties of MFs and promising progress has been achieved [7,14–17]. Wang et al. proposed the incorporation of Cu into the $FeF_2$ crystal lattice by preparing a ternary fluoride of $Cu_{0.5}Fe_{0.5}F_2$. This material exhibits a hysteresis of less than 150 mV with a low cycling rate, achieving high capacity [3]. Following the concept of "ternary fluorides", Gordon et al. successfully synthesized solid solution fluorides including $Ni_yFe_{1-y}F_2$, $Co_yFe_{1-y}F_2$, and $Mn_yFe_{1-y}F_2$, demonstrating that the metal composition determines the formation and growth of the cathode solid electrolyte interphase (SEI) affecting the cathode stability [18]. Later, Villa et al. found that with the substitution of Cu into $NiF_2$, both the volumetric expansion during the first lithiation and the fluorine loss during delithiation are reduced, and thus the cycling performance was improved [19]. These reports show the synergistic effect of metals in the ternary fluorides, which is beneficial for the electrochemical performance of MFs based cathode materials. In general, the synergistic effect of metals can be found more pronounced and is further investigated in high entropy materials (HEMs).

Recently, the use of the high entropy concept to develop materials with tailorable properties is gaining great interest [20–22]. The high entropy concept is derived from high entropy alloys (HEAs), which possess high configurational entropy ($S_{config}$) by incorporating five or more elements into a single-phase structure, leading to the so called "cocktail effect", where the multiple synergies among the constituent elements may result in additional or changed properties. That means HEMs can have the potential to outperform the parent material system [23,24]. Following the high entropy concept, HEMs including different compounds such as oxides [25–27], carbides [28], borides [29], nitrides [30,31], fluorides [22], sulfides [32], and oxyhalides [33] that show unique properties and broad potential applications in various areas, have been prepared. In 2015, Rost et al. gave account of the first high entropy oxide (HEO), demonstrating the entropy stabilization effect [34]. Notably, a HEO with very promising and unexpected properties has been explored as a conversion type electrode material in LIBs. Our previous study depicted that entropy is one of the important factors for the cycling stability of the HEO anode ($(Co_{0.2}Cu_{0.2}Mg_{0.2}Ni_{0.2}Zn_{0.2})O$), probably due to the reduction of some cations, while other cations remain in the rock-salt structure and facilitate the reintegration into the parent structure after conversion [35]. Lökçü et al. indicated that the electrochemical performance of HEOs would be greatly improved by increasing the lithium concentration in the structure of $(MgCoNiZn)_{1-x}Li_xO$ ($x$ = 0.05, 0.15, 0.25, and 0.35) thereby generating more oxygen vacancies [36]. These reports demonstrate the role of chemical disorder, i.e., mixed cations and created vacancies, for the cycling stability and tailorability. Considering of the potential of MFs as high capacity cathodes, it is of great interest to explore conversion mechanism based high entropy fluorides (HEFs) that can be used as cathodes for LIBs.

As previously reported, HEFs were successfully synthesized and investigated for their electrocatalytic properties [37]. In the present work, we report a series of HEFs based materials namely: $(Cu_{1/5}Ni_{1/5}Fe_{1/5}Zn_{1/5}Co_{1/5})F_2$, $(Cu_{1/6}Ni_{1/6}Fe_{1/6}Zn_{1/6}Co_{1/6}Mn_{1/6})F_2$, and $(Cu_{1/7}Ni_{1/7}Fe_{1/7}Zn_{1/7}Co_{1/7}Mn_{1/7}Mg_{1/7})F_2$ as electrode materials for battery applications, in an attempt to exploit their high theoretical specific capacities. It is observed that instead of a step-by-step reduction into each individual metal, HEFs exhibit a single-step reaction process. Moreover, the addition or elimination of an element has a significant effect on the redox potentials while simultaneously reducing the voltage hysteresis during cycling. Moreover, HEFs show reversible lithium storage with high capacities. These findings offer new guidelines for material design and tailoring of electrochemical properties by deliberate selection of elements for high performance LIB cathode materials.

## 2. Experimental

Herein the syntheses of the multi-cation incorporated HEFs via ball milling process is described. Solid solutions of 4, 5, 6, and 7 elements containing HEF nano-powders were synthesized via high energy mechanochemical milling process. Equimolar weighted ratios of the respective binary fluorides $CuF_2$ (99.5%, Alfa Aesar), $CoF_2$ (98%, Abcr GmbH), $NiF_2$ (97%, Alfa Aesar), $ZnF_2$ (99.995%, Abcr GmbH), $MnF_2$ (99%, Abcr GmbH), $FeF_2$ (98%, Alfa Aesar), and $MgF_2$ (99.99%, Alfa Aesar) were mixed and ball milled at 500 r/min for 24 h using a Retsch PM100 planetary ball mill. The ball-to-powder weight ratio was 40:1. WC vials and WC balls (7 mm in diameter) were used. All the starting precursors were analytical grade and used without further purification. For comparison, all binary fluorides were ball milled under the same conditions.

### 2.1. Electrochemical characterization

HEF/MWCNT was obtained by mechanochemical milling (6 h) with 15 wt% multi-walled carbon nano-tubes (MWCNT, Sigma Aldrich, 7.5% MWCNT basis, outer diameter of 7–15 nm, length 0.5–10 μm) and 85 wt% HEF powder (active material). After the milling, HEF/MWCNT nanocomposites were collected in Ar-filled glovebox. Electrodes were prepared by slurry coating of 80 wt% cathode material (HEF/MWCNT), 10 wt% carbon black (C65), and 10 wt% polyvinylidene fluoride (PVDF, Solef 5130, Solvay) in *N*-methyl-2-pyrrolidone onto aluminium foil. The electrodes were dried overnight at 100 °C. All electrode tapes with an areal loading of around 0.5–1 mg/cm$^2$ were prepared in Ar-filled glovebox to avoid exposure to air.

Electrochemical testing was done with CR2032 type coin cells. All cells were assembled inside an Ar-filled glovebox and comprised an HEF7 composite cathode, a GF/D glass microfiber separator (GE Healthcare Life Science, Whatman), and a lithium anode (China Energy Lithium Co., Ltd) of diameters 13 mm, respectively. LP57 [1 M $LiPF_6$ in 3:7 (*w*/*w*) mixture of ethylene carbonate (EC) and ethyl methyl carbonate (EMC)] was used as electrolyte. Cyclic voltammetry (CV) and electrochemical impedance spectroscopy measurements (EIS) were performed using a BioLogic VSP-300 potentiostatic device. The impedance data were acquired by applying 10 mV alternating current (AC) perturbation signal over frequency range of 1 MHz to 1 Hz (20 points/decade). Symmetric cells were constructed by sandwiching two HEF/MWCNT electrodes separated by two sheets of GF/C separators. GF/C was wetted with 200 μL LP57. EIS experimental plots were fitted by using *Z*-view software (Scribner Associates, Southern Pines, NC).

### 2.2. Structural characterization

#### 2.2.1. Operando XRD

X-ray diffraction (XRD) patterns of all HEF based electrodes and pristine powders were measured with STOE Stadi P diffractometer, equipped with a Ga-jet $K_\beta$ radiation source ($\lambda$ = 1.208 Å). Operando XRD measurements were conducted on the HEF7 electrodes at different states of charge (SOC) to probe the reaction mechanism. For this purpose, the HEF7 slurries were casted on the carbon paper

current collector with an active material loading of 7 mg in an argon-filled glovebox.

*2.2.2. SEM*

The microstructures of the pristine HEF nanoparticles and HEF/MWCNT composites were examined via a scanning electron microscope (SEM) Leo 1530 operated at 5 kV acceleration voltage with 4 mm as working distance.

*2.2.3. Ex-situ TEM*

High-resolution transmission electron microscopy (HR-TEM), selected area electron diffraction (SAED), energy dispersive X-ray (EDX) spectroscopy data were collected using a Field Electron and Ion Company (FEI) Titan 80–300 microscope, equipped with a CEOS image spherical aberration corrector, a HAADF-STEM detector (Fischione model 3000), EDAX SUTW EDX detector, and a Tridiem Gatan image filter. An accelerating voltage of 300 kV was used. The powder samples were dispersed on a lacey gold grid and loaded onto a FEI double tilt holder. All TEM sample preparations were carried out inside Ar filled glovebox. For ex-situ characterization, the electrodes of lithiated and delithiated samples were rinsed with dimethyl carbonate and dried inside inert gas filled glovebox.

*2.2.4. Ex-situ XPS*

X-ray photoelectron spectroscopy (XPS) measurements were performed on a *K*-Alpha+ instrument (Thermo Fisher Scientific) with a monochromatic Al-$K_\alpha$ X-ray source (1486.6 eV) and 400 μm spot size. The *K*-Alpha+ charge compensation system was applied to prevent localized charge build-up during analysis using 8 eV electrons and low-energy Ar ions. Data acquisition and processing were carried out using the Thermo Avantage software [38,39] The spectra were fitted with one or more Voigt profiles. The binding energies were calibrated with respect to the C 1*s* peak of hydrocarbons at 285.0 eV. The analyser transmission function, Scofield sensitivity factors [40], and effective attenuation lengths (EALs) for photoelectrons were applied for quantification. EALs were calculated by using the standard TPP-2 M formalism [38].

*2.3. Computational method*

Spin-polarized density functional theory (DFT) calculations were performed using the plane-wave Quantum-ESPRESSO software package [39]. The ultrasoft pseudopotential was applied to represent the core electrons [41]. The generalized gradient approximation (GGA) – revised Perdew-Burke-Ernzerhof (PBEsol) exchange-correlation functional was chosen to optimize the geometries and unit cells as it has been shown to be an appropriate functional to predict the structural parameters of solids [42]. The Hubbard-U correction by Cococcioni et al. [43] was added to correct the self-interaction error in the strongly correlated 3*d* electrons for the calculation of density of state (DOS). The U values of 6.2, 3.32, 2.5, 5.3, and 5 eV were considered for Ni, Co, Mn, Fe, and Cu, respectively. A cuttoff energy of 680 eV was applied for the plane-wave basis set. For the structural optimization (relaxation) calculations, the energy and force convergence threshold were set to $6.8\times10^{-3}$ and $6.8\times10^{-2}$ eV/Å, respectively. A stress tolerance of 0.5 Kbar and a smearing of 0.1 eV were applied. The disordered structures were represented by special quasi-random structures (SQSs) [44], which has been shown to have comparable results as cluster expansion (CE) [45]. The atomic distribution of SQSs is chosen such that the cluster correlations of neighbouring atoms are as close as the expected random atomic arrangement for a given structure size. In this work, the disordered structures were generated by the mcsqs code implemented in the Alloy Theoretic Automated Toolkit (ATAT) package [46]. All three systems, namely HEF5, HEF6, and HEF7, were modeled with the rutile-type structure with the *P42/mnm* space group. To have a reasonable correlation with respect to the composition in SQSs, the following supercell size and number of atoms were applied: a $2\times2\times5$ supercell containing 120 atoms/cell for HEF5, and a $2\times3\times7$ supercell containing 252 atoms/cell for HEF6 and HEF7. A *k*-point sampling mesh of $1\times1\times1$ was used for the structural relaxation of the three systems. For the DOS calculation, a *k*-point mesh of $2\times2\times2$ for HEF5 and $2\times2\times1$ for HEF6 and HEF7 systems was applied.

## 3. Results and discussion

HEFs were synthesized by a mechanochemical method as in our previous work [37], $(Cu_{1/5}Ni_{1/5}Fe_{1/5}Zn_{1/5}Co_{1/5})F_2$, $(Cu_{1/6}Ni_{1/6}Fe_{1/6}Zn_{1/6}Co_{1/6}Mn_{1/6})F_2$, and $(Cu_{1/7}Ni_{1/7}Fe_{1/7}Zn_{1/7}Co_{1/7}Mn_{1/7}Mg_{1/7})F_2$ are marked as HEF5, HEF6, and HEF7, respectively, in the following sections. For comparison, medium entropy materials of $(Cu_{1/4}Ni_{1/4}Fe_{1/4}Zn_{1/4})F_2$ and $(Cu_{1/3}Ni_{1/3}Fe_{1/3})F_2$ (named as MEF4 and MEF3, respectively) were also synthesized. Fig. 1(a) shows the schematic illustration of the synthesis process utilized (further details are given in the Experimental Section). The $S_{config}$ for each MEF and HEF is calculated according to Eq. S1 and presented in Table S1. Typically, materials with $S_{config}$ of greater than 1.5*R* can be considered as HEMs, lower than 1*R* as low entropy materials, and with $S_{config}$ between 1*R* and 1.5*R* as medium entropy materials [24]. Due to the intrinsic low electronic conductivity of fluorides, the HEFs were further mixed with MWCNT and ball milled at 500 r/min for 3 h to obtain the HEF/MWCNT composites. SEM images of HEF powder and HEF/MWCNT composite are presented in Fig. 1(b and c), showing that powders are in nano to micrometer size range and intertwined with MWCNTs. As reference materials, all metal fluorides (MFs) were ball milled separately for 24 h and then mixed with MWCNT.

*3.1. Electrochemical performance in lithium battery cells*

To investigate the electrochemical redox potentials, CV measurements were performed. In order to evaluate the electrochemical differences of high entropy compounds, where all elements are on the same lattice, to simple mixtures of MF compounds, a series of experiments were conducted. CV profiles of the HEF, MEF, mixture of all MFs, and each individual MF are given in Fig. 2(a–f) and Fig. S1. In the mixed fluorides system (Fig. 2f), several redox peaks were observed during the de/lithiation process, which indicates that the reactions for each fluoride compound tend to occur independently. However, the lithiation/delithiation processes for HEFs and MEFs show significant differences from that of mixed fluorides. Comparable lithiation behavior was observed in all HEFs and MEFs. For instance, during the first lithiation process, two reduction peaks at ~1.9 and 1.5 V could be observed for all materials (Fig. 2a–e). The small peak at 1.5 V is probably related to the decomposition of electrolyte with the formation of the SEI layer [47]. In the subsequent lithiation processes, only one reduction peak was observed. In contrast to the lithiation process, there were significant differences in the delithiation process between the HEFs and MEFs. For the HEFs, only one oxidation peak was observed at 3.5, 3.25, and 3.05 V for HEF5, HEF6, and HEF7, respectively. In the case of the MEF4 and MEF3, two distinct peaks occurred around 2.9 and 3.5 V during delithiation (see Fig. 2d and e). A similar behavior as for MEF4 and MEF3 has already been observed by Wang et al. for a two-metal-based fluoride system ($Fe_{0.5}Cu_{0.5}F_2$), where the two lithiation and delithiation reaction steps correspond to the transition of $Cu^{2+}/Cu^0$ and $Fe^{2+}/Fe^0$ [7].

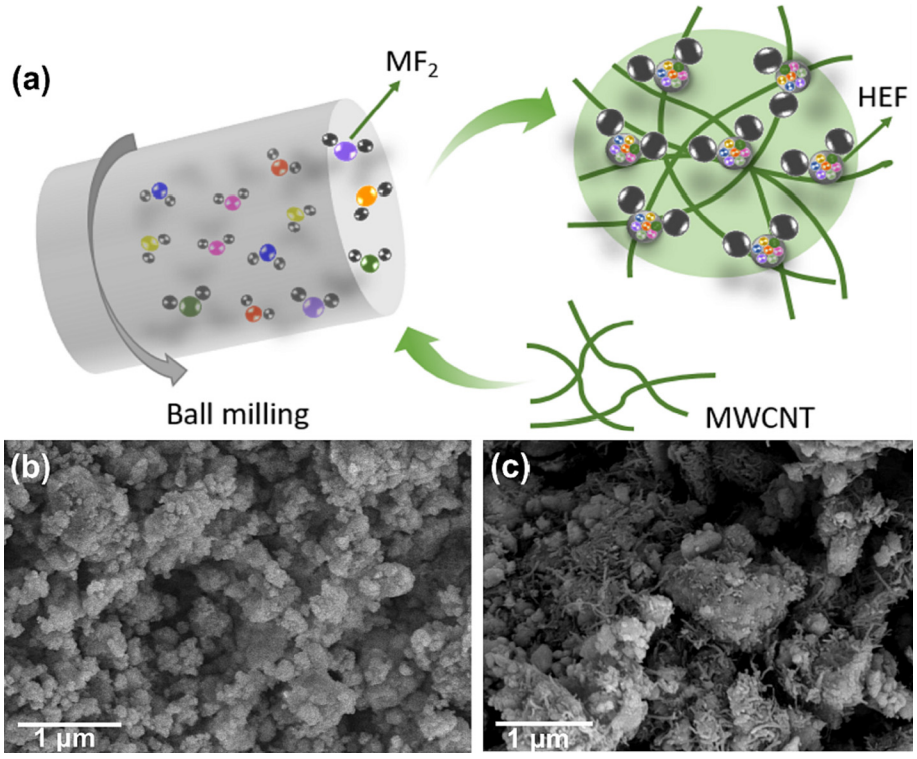


**Fig. 1.** (a) Schematic diagram of the synthesis processes for the HEF/MWCNT composites, where MF represents the binary fluorides of $CuF_2$, $NiF_2$, $FeF_2$, $CoF_2$, $ZnF_2$, $MnF_2$, and $MgF_2$ in equimolar ratio. Typical SEM images of (b) HEF powder and (c) HEF/MWCNT composite after 3 h of ball-milling.

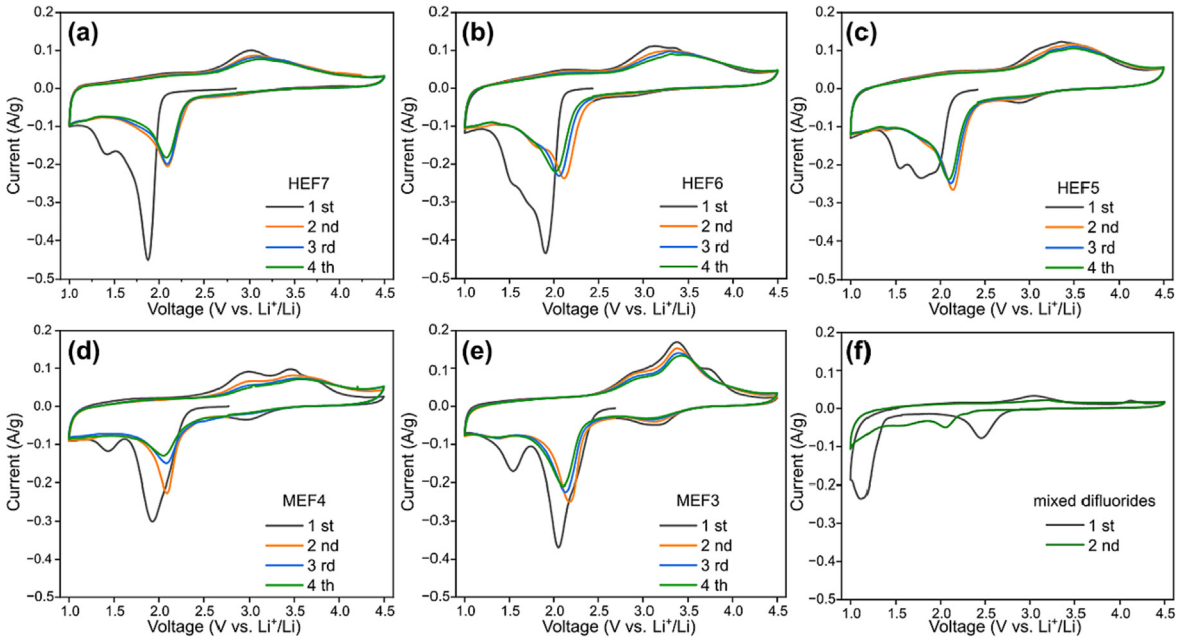


**Fig. 2.** Cyclic voltammograms of (a) HEF7, (b) HEF6, (c) HEF5, (d) MEF4, (e) MEF3, and (f) mixture of all binary fluorides ($CuF_2$, $NiF_2$, $FeF_2$, $CoF_2$, $ZnF_2$, $MnF_2$, and $MgF_2$) measured in the voltage range of 1.0–4.5 V vs. $Li^+/Li$ with a scan speed of 0.1 mV/s.

Accordingly, it can be assumed that in the case of MEF3 and MEF4 similar conditions exist and that firstly one of the metal species reacts with Li, while the others are not yet or not at all involved in the reaction. This will be investigated in more detail below using XPS. As mentioned above, in the case of HEFs, it then appears that the lithiation/delithiation process is a simple one-step reaction. This will be discussed in the XRD and TEM sections. However, we would like to point out that it cannot be excluded that within the broad oxidation peak of the HEFs, several individual reactions belonging to the transition metals may occur separately, and that due to the low concentration of the individual elements this may only be represented in a broad peak. Nevertheless, a continuous shift of the maximum of the oxidation peak from 3.5 (HEF5) to 3.25 (HEF6) to 3.05 V (HEF7) can be observed. It can therefore be

assumed that the addition or elimination of an element influences the redox potentials. This paves the way for tailoring the reaction potential and adjusting the electrochemical behavior by changing the elemental composition of the electrode active material.

The galvanostatic rate capability performance of MEF4, HEF5, HEF6, and HEF7 at different currents is given in Fig. 3(a). During the rate performance test, HEF7, HEF5, and MEF4 initially show comparable discharge capacities, while HEF6 shows higher capacities at currents of 25 and 50 mA/g. However, as the current increases (100 mA/g), HEF7 shows increasingly better performance and even after returning to 50 mA/g, it exhibits the highest discharge capacities (~300 mAh/g). The same was also observed for the long cycling performance at 50 mA/g (Fig. 3b). Each HEF sample could yield a discharge capacity of more than 400 mAh/g for the first five cycles at 25 mA/g and then retain more than 100 mAh/g after 80 cycles at 50 mA/g. Whereas the metal fluorides ($CoF_2$, $NiF_2$, $CuF_2$, $MgF_2$, $MnF_2$, and $ZnF_2$) as well as the MEF4 shows a capacity of <100 mAh/g after 80 cycles (Fig. S2 and Fig. 3b). MEF4 shows a strong capacity decay compared to HEFs, which also indicates the cycling stability of the HEFs. Although HEF7 has the lowest initial capacity, it shows the highest specific capacity of ~190 mAh/g after 80 cycles. In addition, it is noted that HEF7 shows improved performance compared with HEF6, even though Mg is inactive in the given potential range, which will be discussed in more detail in the XPS part. In order to investigate the better performance of HEF7 in more detail, the total electron density of the states (DOS) was calculated using DFT. The DOS calculated by DFT for the HEF systems showed a band gap of ~2.2 eV for all three systems (Fig. S3), with no significant deviation. A gap state between 0 and 0.8 eV is observed for the systems, which is related to the *d* band of Cu (see the projected DOS in the Fig. S3). This shows a strong tendency of Cu to be reduced from 2+ to 1+. Although the major contribution of valence band maximum (VBM) is from the Fe-*d* states in the HFE5 system, it is dominated by Mn-*d* in the HFE6 and HEF7 systems (Fig. S3). This clearly shows that Mn has the highest tendency, compared to the other elements, to be oxidized to 3+ and perhaps 4+. This is in line with the previous studies showing a large charge state of 4+ for Mn in the fully-discharged $LiNi_xCo_yMn_{1-x-y}O_2$ (NCM) cathodes [48,49]. As expected, no significant change in the DOS is observed after adding Mg to the HEF6 compound. This is because Mg has only strongly localized *p* states that are located far away from the Fermi level. According to previous reports, increasing the number of metal species improves the lithium transport properties [20], so we speculate that the increase in the disorder in the high entropy fluoride may improve the lithium conductivity of this system. Thus, the electrochemical properties of this system were improved with the increase in the number of metals. Moreover, the HEF7 electrode maintains a discharge capacity of 125 mAh/g after 100 cycles and a high Coulombic efficiency of ~99% even under fast cycling conditions (Fig. 3c). It can be seen that in the voltage profiles of HEF7 and $FeF_2$ (Fig. 3d) as well as the average voltage hysteresis of HEF7 and $FeF_2$ (Fig. S4), HEF7 exhibits the lower overpotential between charge and discharge process. Moreover, HEF7 shows a higher discharge voltage than $FeF_2$, which would benefit energy density of the battery. The high specific capacity explains that the HEF-based electrodes presumably undergo conversion mechanisms as the binary fluorides [50]. Since HEF7 shows the best capacity retention/stability, it will be discussed in more detail in the following.

### 3.2. Electrochemical impedance spectroscopy

EIS is a fundamental technique to define the diffusion process, the charge transfer kinetics, and the electrolyte-electrode resistance [51]. To gain more information about the conductivity properties of the HEF7 electrodes, EIS measurements were performed. To recognize the individual process contributing to the EIS response, first, two-electrode cells in symmetric cell configuration (identical HEF7/MWCNT composite electrodes) were prepared. Standard electrolyte (LP57) was utilized for all the EIS tests. Additionally, reasons responsible for capacity fading have been drawn from the EIS results of the cycled cells.

Fig. 4 shows the Nyquist plots of the HEF7 electrode in a symmetric cell (Fig. 4a) and in a half-cell configuration (Fig. 4b) along with the respective equivalent circuits used to analyze the EIS data. The continuous lines in Fig. 4 show the fitting curves and dots represent the recorded experimental data. In general, the EIS of a half-cell provides information about the working electrode and the counter electrode, and it is difficult to separate the respective contributions to the spectrum, e.g., charge transfer between each electrode and the electrolyte. The EIS information of a symmetric cell consisting of two identical electrodes can eliminate the influence of the counter electrode and thus allow a more direct investigation of the electrode material and interfacial properties against the electrolyte [52]. The EIS spectrum of the symmetrical cell of HEF7 (Fig. 4a) is composed of a depressed semicircle in the high frequency region and a sloping straight line feature in the low frequency region. The real part of the impedance is denoted as *R*1 in the equivalent circuit, which may arise from the electrolyte resistances. The first semicircle in the high frequency region may be attributed to the charge transfer resistance between the cathode-electrolyte (*R*2) [53]. The straight line shown in the low-frequency region can be represented by constant phase element (CPE2), which shows the blocking nature of $Li^+$ diffusion on the cathode side.

Fig. 4(b) shows the EIS data from HEF7/MWCNT composite electrode with Li counter electrode in a half-cell configuration. From these EIS spectra, the experimental data of electrodes (denoted by points) show a prominent blocking feature (at low frequencies) and two flattened high and medium frequency semicircles. The changes in the first high-frequency semicircles in the cycled EIS electrode can be caused by the SEI layer formation at the cathode surface. These semicircles of the half-cell configuration in Fig. 4 (b) are similar to the counterpart presented in symmetrical cell spectrum ($f_{max}$ = 27 kHz) with an additional influence from the SEI formation during cycling. The second semicircle in the medium frequency region can be ascribed to the charge transfer resistance caused at the anode/electrolyte interface (*R*2). In the composite structure, better interfacial contact between the active material and MWCNT could be anticipated due to the porous structure of MWCNT. The derived parameters from the equivalent circuit model fitting performed with the *Z*-view software can be found in Table S2. Due to the overlapping of the high and medium frequency semicircles of the half-cell measured at open circuit voltage, the absolute quantification of the equivalent circuit components was quite cumbersome. Nevertheless, with progressing cycle number from 5 up to 50 cycles it is evident that the SEI formation plays a significant role in increasing the charge transfer resistance on the cathode side, while further cycling results in a decrease in resistance. A more notable resistance increase is observed for the medium frequency semicircle attributed to the charge transfer to the Li anode. This increase might even play a more significant role in the observed capacity fading. The degradation of the anode surface might be due to the elemental dissolution from the active material through the electrolyte and their presence at the electrolyte/anode interface, which was detected by means of (EDX (Fig. S5). In addition, the slope of the straight line in the low frequency region decreases with the increase of the cycle number, indicating the decrease in the capacitive nature of the electrode and increased resistive component. This may be due to the volume change of the active material during cycling and the resulting poor

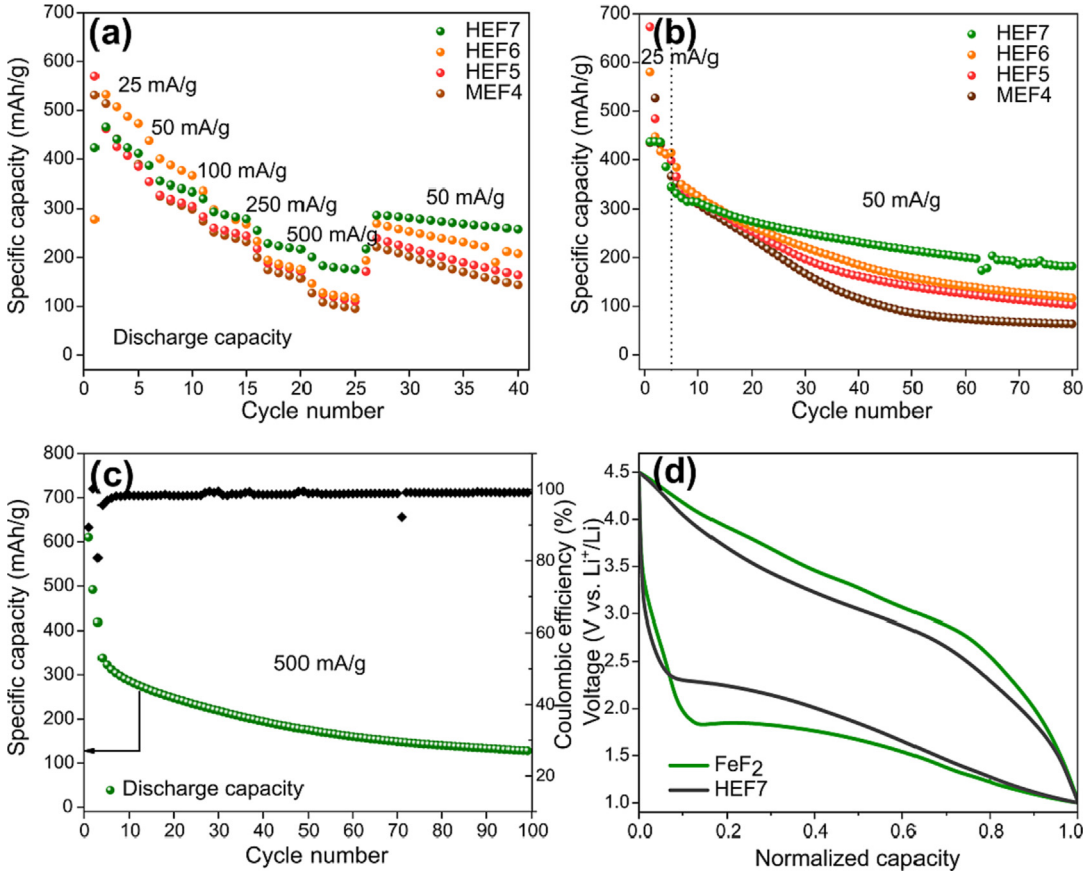


**Fig. 3.** (a) Galvanostatic rate capability performance of MEF4, HEF5, HEF6, and HEF7 at different currents and (b) Cycling capacity at 25 and 50 mA/g measured in the voltage range of 1.0–4.5 V. (c) Cycling performance of HEF7 at 500 mA/g. (d) Comparison of normalized capacities of HEF7 and $FeF_2$ in the voltage range 1.0–4.5 V at 50 mA/g.

contact between the particles, causing higher resistance for both $Li^+$ and electron transport.

### 3.3. Structural evolution during cycling

In order to have a better understanding of the reaction mechanism observed in HEF based materials and structural changes in the reversible de/lithiation processes, a comprehensive characterization implementing XPS, XRD, and TEM was performed.

XPS analyses were performed on HEF material in the initial, discharged, and charged states (Fig. 5). A summary of the results is presented in Table S3. Cu ions in the pristine electrode show two peaks at around 944 and 937 eV, which could be attributed to the $Cu^{2+}$ main peak and satellite of Cu $2p_{2/3}$ respectively (Fig. 5a). The third peak at lower binding energy (~933 eV) can be attributed to either $Cu^{1+}$ or $Cu^0$. The Cu peak is no longer $Cu^{2+}$ and stays in the reduced state at the binding energy of around 933 eV after discharge. The Cu LMM peak of HEF7 is overlapped with Zn LMM with low intensity. Nevertheless, it can be inferred from the spectra of charged and discharged electrodes (Fig. 5a and b) that Cu is involved in the reaction. Narrow Zn $2p_{3/2}$ peak consistently appears at around 1023 eV; however, the binding energies of $Zn^{2+}$ and $Zn^0$ are very close to each other and the analysis of Zn LMM auger peak (Fig. 5d) is required. The Zn LMM peak at 990 eV at the lithiated electrode indicates the emergence of metallic Zn; then the peak shifts mainly back to 985 eV at the delithiated electrode and can be attributed to the $Zn^{2+}$ regenerate. The analysis of Fe 2*p* ions (Fig. 5e) is hampered due to the overlap of Ni and Co auger peaks resulting in high background intensity of Fe 2*p* region. The Ni ions also overlap intensively with F KLL auger peaks, which makes their analyses difficult. However, the comparison of the spectra in Ni 2*p* region (Fig. 5f) shows the emergence of a small shoulder at around 853 eV in the discharged (lithiated) electrode that could probably be attributed to the metallic Ni. This small shoulder is indicated by an arrow and disappears again after delithiation (charged state), therefore potentially suggesting reversibility for $Ni^{2+}$ formation by delithiation [54,55]. The Mn ions in the pristine electrode can be attributed to the $Mn^{2+}$ ions, according to the provided peak deconvolution in Fig. 5(h) that shows the multiplet splitting of $Mn^{2+}$. The metallic Mn $2p_{3/2}$ and Mn $2p_{1/2}$ peaks appear normally at low binding energies at around 639 and 648 eV [56]. The peak positions show some slight negative shifts for the discharged states in comparison with the pristine electrode with the appearance of a peak at 647 eV and a small shoulder at 660 eV, indicating the reduction of $Mn^{2+}$ into Mn metal phases during the discharging processes [57,58]. The spectra of Co ions in pristine and charged electrodes (Fig. 5g) show the characteristic satellite of $Co^{2+}$ ions is around 6 eV higher than the main peak (indicated by an arrow in Fig. 5g); however, their low intensity, mainly in the cycled electrodes, makes peak assignment difficult. The emergence of a small shoulder at around 778.5 eV in the discharged (lithiated) Co $2p_{3/2}$ spectra might indicate the reduction of Co ions to metallic Co upon lithiation [59]. Mg 1*s* peak (Fig. 5i) appears at around 1305 eV and remains consistent in all of the electrodes. Its binding energy can be attributed to $Mg^{2+}$ ions, whereas the metallic Mg normally appears at around 1303 eV. Therefore, Mg is not involved in the reduction or oxidation process. Fluoride ions in the structure of HEF7 appear at around 685.5 eV (Fig. 5j), whereas the polyvinylidene fluoride (PVDF) peak appears at around 688 eV. In F 1*s* spectra, also the contribution of electrolyte degradation products can

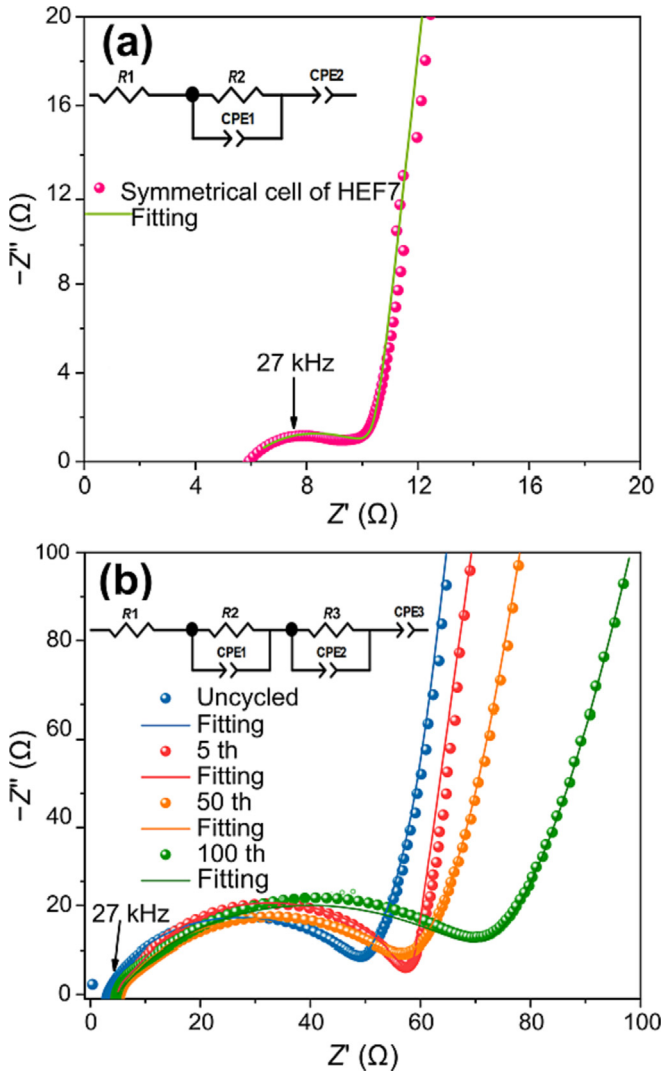


**Fig. 4.** (a) Electrochemical impedance spectra of symmetrical cells with HEF7 electrodes, inset equivalent circuit for fitting the experimental data (where *R*1 and *R*2 denote the resistances, CPE1 and CPE2 denote the constant phase elements). (b) Nyquist plots for the HEF7 at pristine state, after 5 cycles, 50 cycles, and 100 cycles, inset is equivalent circuit model used for fitting the experimental data (where *R*1, *R*2, and *R*3 denote the resistances, CPE1, CPE2, and CPE3 denote the constant phase elements). Table S2 shows the equivalent circuit values of the fitting components obtained from the equivalent circuit models.

be found. However, the binding energy difference between Li-F and M-F is too miniscule to distinguish. Therefore, the peak in F 1*s* between discharged and charged sample is observed to slightly change. Nevertheless, we can infer that Li-F and M-F are generated after discharge and charge, respectively. In summary, with the exception of Mg, differences between the oxidation states in the different states (pristine, discharged, and charged) can be identified for all elements, suggesting a redox reaction during cycling. In the case of Mg, it can be assumed that it may have a stabilizing effect on the system due to the non-reaction. A similar behavior has already been observed for HEO [(CoCuMgNiZn)O], in which a stabilization matrix structure was formed by the species that were not involved in the conversion reaction [35]. Possibly, the better stability for HEF7 can be explained by a comparable mechanism. Further structural investigations by means of XRD and TEM should provide more information.

Operando XRD was performed to shed light on the possible conversion mechanism occurring during cycling. Ga-jet $K_\beta$ X-ray source with adjusted optics was used to achieve high intensities with limited sample volume. Fig. 6 shows voltage profiles (1st discharge/charge and 2nd discharge) together with the evolution of the reflection position and the contour plot for HEF7. As shown in Fig. 6(a), the discharge reaction begins at an open circuit voltage of 3.1 V, a rapid voltage drop to 1.86 V (inset image of Fig. 6a) follows. As reported by Xiao et al., this drop could be ascribed to the pseudo-intercalation of $Li^+$ into the structure and possible disproportionation of metal compounds to form $Li_x$HEF7, which remains its initial rutile structure [60–62]. Afterwards, a significant recovery of the voltage occurs before the flat operating voltage at ~1.95 V, indicating the onset of the conversion reaction appears [62]. The intensity of the HEF7 reflection at 41° is observed to increase and then shift to 41.3° (Fig. S6) during lithiation. Moreover, the intensity of the reflections associated with the initial rutile-type structure becomes weaker as the lithiation progresses, while a new broad reflection at 34° is observed. This new reflection (34°) could belong to a rock-salt structure arising from the formation of nano-sized metal species and possibly metal-substituted LiF as reported for $FeF_2$. Further, the formation of an undetectable amorphous phase during lithiation might be possible [41]. With ongoing lithiation, the reflections from the initial rutile structure disappear and do not reappear after delithiation. This behavior is typical for conversion materials and might result from the formation of small crystallites below the detection limit of XRD [3,63]. Therefore, TEM is used for further characterization.

Fig. 7 shows the ex-situ TEM images of electrochemically lithiated (Fig. 7a) and delithiated (Fig. 7c) HEF7 (1.0 and 4.5 V, respectively), and their corresponding SAED patterns (Fig. 7b and d). At this point we would like to mention that the crystallinity of the discharged sample is very low, so there are only a few diffraction rings to index the structure. On the other hand, there are too many possible candidates, which a reflection can be indexed to. Nevertheless, SAED reveals that the initial HEF7 electrode material was electrochemically reduced to a solid solution of transition metals with LiF after lithiation (discharged to 1.0 V) (Fig. 7b). EDX-mapping shows a homogeneous distribution of the elements in the nanoscale after lithiation, with no agglomeration or segregation present (Fig. 7e). Besides, the Mg is also uniformly distributed in the discharged sample, suggesting that unreacted Mg containing compound ($Mg^{2+}$), possibly within the dominant amorphous phase, is uniformly distributed in the mixture of metal alloy and LiF, possibly metal-substituted. After delithiation of the HEF7 electrode to 4.5 V, the majority of areas in the HR-TEM image (marked in Fig. 7c) show lattice spacing of ~0.33 nm. This is a clear indication that *d*-spacing corresponds to the (110) plane of the parent rutile phase. Following the SAED after delithiation (Fig. 7d), the rutile structure is partially reformed. However, the ring of (120) is observed to be broadened and a small diffraction signal appeared at 4.05 1/nm in the corresponding profile of the SAED pattern (Fig. S7) which could be caused by the overlap between (111) of fcc metal and (110) of bcc metal, indicating that unreacted metal solid solution remained in the charged sample. It was also observed in XRD that the intensity of the peak appearing at 34° did not disappear completely after delithiation process was completed, thus also indicating the presence of unreacted metal particles in the material. This indicates that the metal does not fully convert to fluoride during delithiation, which could be ascribed to the poor contact resulting from the volumetric change during the conversion process. During the delithiation process, the reformation of high entropy compounds breaks the conductive network formed by metals, which impedes the reaction leading to capacity fading. It can be inferred from CV and XPS results that HEFs solid-solution phase has been reformed after $F^-$ transfer from LiF to the transition metals solid solution. This evidence combined with

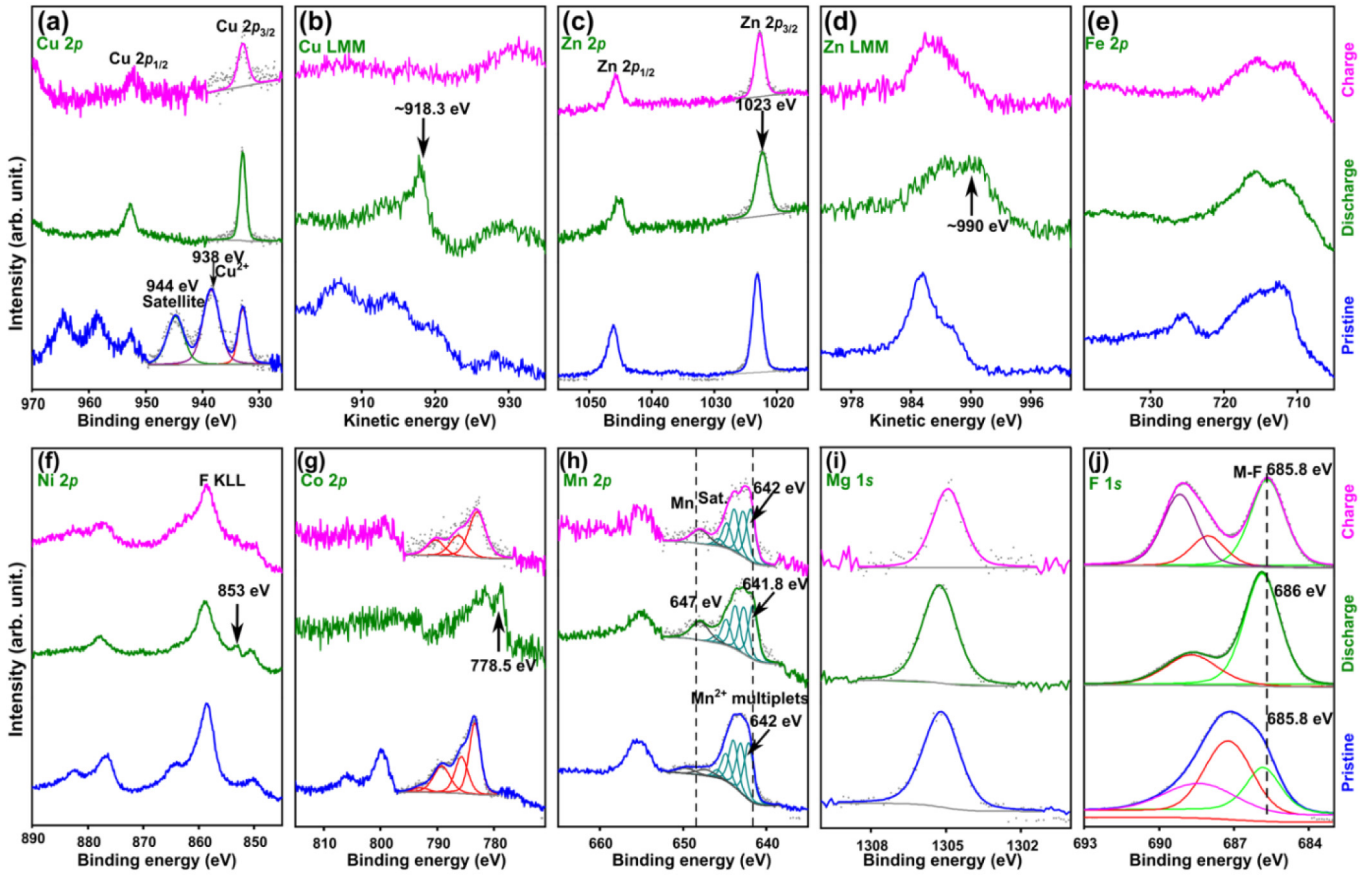


**Fig. 5.** XPS spectra of (a) Cu 2*p*, (b) Cu LMM (c) Zn 2*p*, (d) Zn LMM, (e) Fe 2*p*, (f) Ni 2*p*, (g) Co 2*p*, (h) Mn 2*p*, (i) Mg 1*s*, and (j) F 1*s* of pristine electrode (blue), first lithiation electrode (green), and first delithiation electrode (pink).

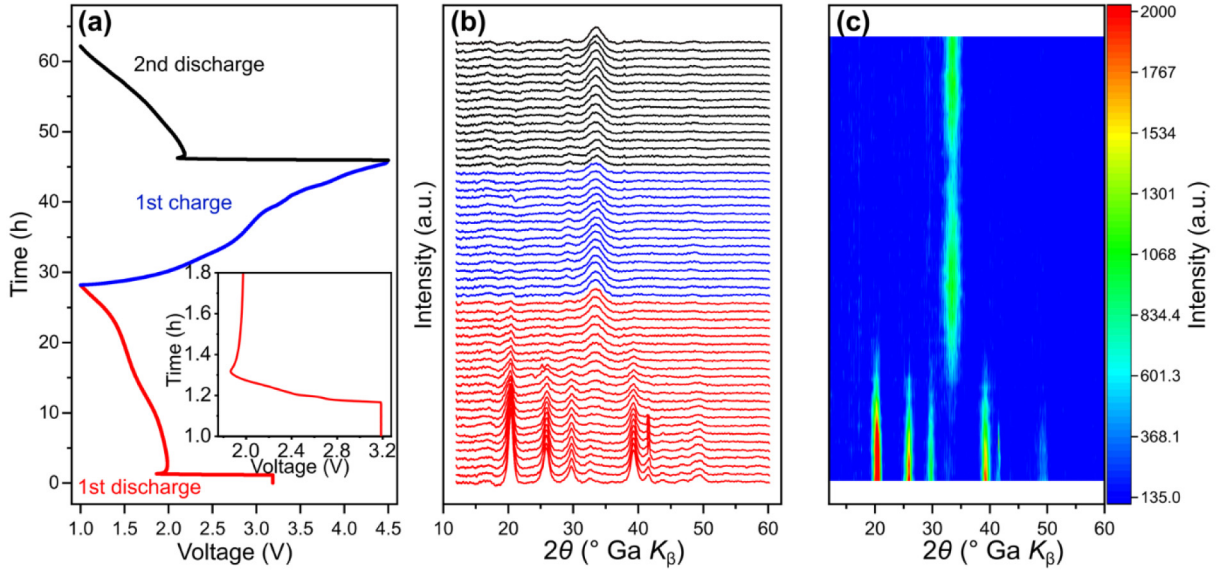


**Fig. 6.** Operando XRD patterns (b) collected during the first discharge and charge process at a current density of 50 mA/g (a), and corresponding contour map (c).

the operando XRD pattern (Fig. 6), confirm a conversion reaction mechanism presenting in the HEF based materials. The occurrence of the continuous network of metallic nano domains can be beneficial as an internal conductive network. This can facilitate the conversion kinetics and voltage polarization, thereby improving the overall electrode cycling performance. The continuity of this network however needs to be remained throughout lithiation and delithiation to achieve its maximum effect.

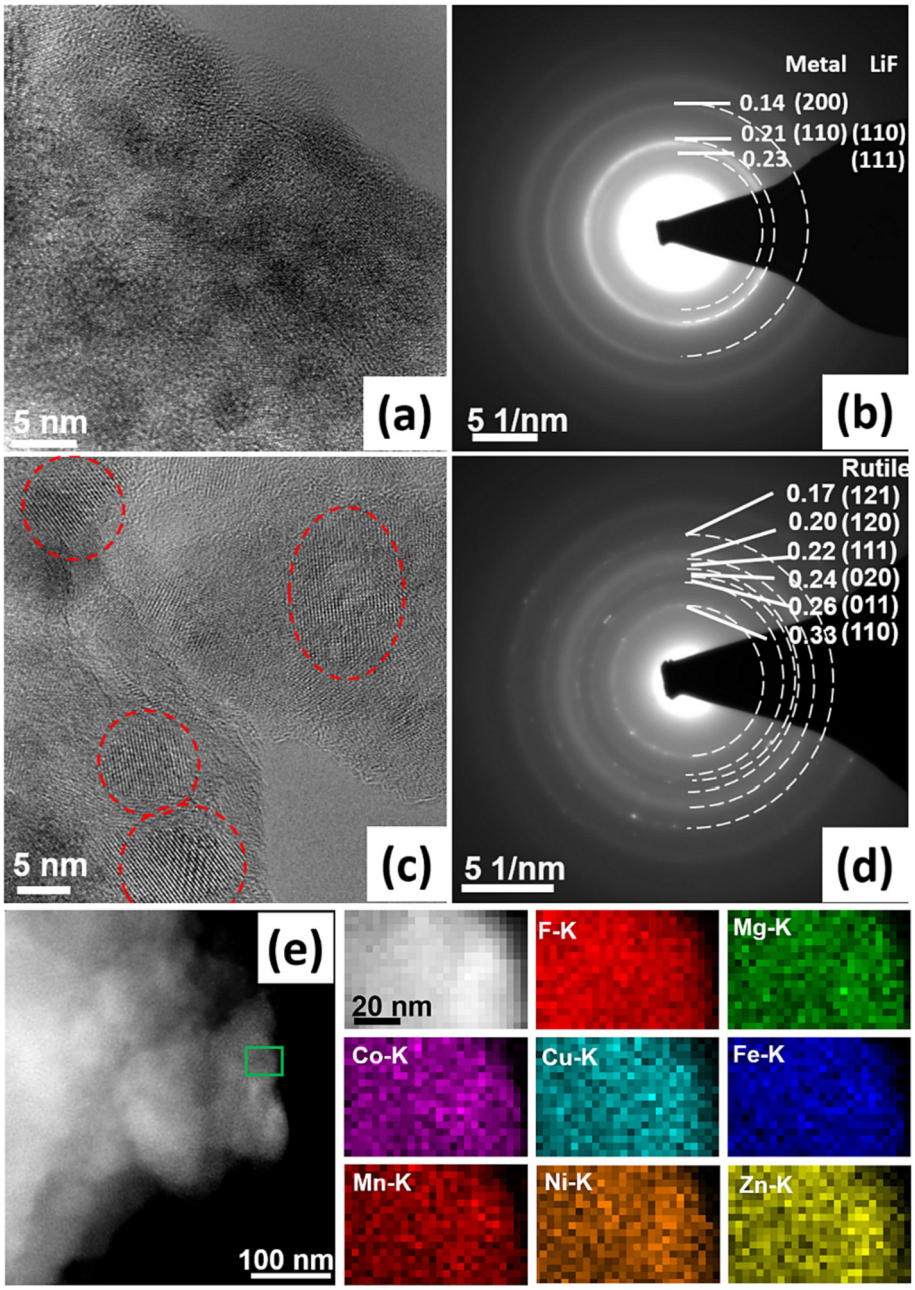


**Fig. 7.** HR-TEM images of various cycled HEF7 electrodes after lithiation to 1.0 V (a), delithiation to 4.5 V (c), and their corresponding SAED patterns in panels (b) and (d), respectively (all values of *d* spacing illustrated in SAED are given in nm). (e) EDX-mapping after 1st discharge.

## 4. Conclusions

In summary, HEFs are demonstrated as high-capacity cathode materials for lithium-ion batteries. It is proposed from the lithiation/delithiation process that the electrochemical activity of HEFs based materials could be tailored by simply changing the constituent elements. With in-depth characterization of the electrodes by ex-situ XPS, operando XRD, and ex-situ HR-TEM techniques, it has been revealed that the solid solution of transition metals is present in the lithiated phase together with a substantial amount of amorphous phase and possibly metal-substituted LiF. The rutile HEFs phase could be partially restructured after delithiation. HEF with seven metal elements exhibited high capacity at the beginning of cycling process. More importantly, HEF7 maintained a moderate cycling performance with a capacity of more than 125 mAh/g after 100 cycles at a high specific current of 0.5 A/g. As a future perspective, the potential advantages of HEFs can be further improved. One approach is constructing a composite electrode consisting of nanostructured HEFs particles whose size must be comparable to the length scale of the conversion reaction and directly connected to electrically conductive scaffolds. The other approach is coating the material to preserve metal ions dissolution into the liquid electrolyte and onto the lithium anode to benefit the cycling stability. The conversion mechanism of HEF7 needs to be further investigated to determine the underlying reactions contributing to the enhanced electrochemical performance.

## Declaration of competing interest

The authors declare that they have no known competing financial interests or personal relationships that could have appeared to influence the work reported in this paper.

## Acknowledgments

Y.C. and P.A.S contributed equally to this work. Y.C. acknowledges the financial support received from the China Scholarship Council (CSC). P.A.S. acknowledges MERAGEM graduate school and the Ministry of Science, Research and Arts of the State of Baden-Württemberg for funding research. M.B. acknowledges the support of the German Research Foundation (DFG) project (SE 1407/4-2). Q.S., B.B. and H.H. thank the support of the EnABLES, a project funded by the European Union's Horizon 2020 research and innovation program under grant agreement (730957). S.S., M.B. and H.H. also acknowledge the support of EpiStore project under grant agreement (101017709). Authors acknowledge the Centre for Electrochemical Energy Storage Ulm-Karlsruhe (CELEST). The authors acknowledge the support from the Karlsruhe Nano Micro Facility (KNMF), the Helmholtz research infrastructure at Karlsruhe Institute of Technology (KIT) for the access to microscopy.

## Appendix A. Supplementary data

Supplementary data to this article can be found online at https://doi.org/10.1016/j.jechem.2022.05.032.

## References

[1] A. Manthiram, Nat. Commun. 11 (2020) 1550.
[2] F. Wu, G. Yushin, Energy Environ. Sci. 10 (2017) 435–459.
[3] F. Wang, R. Robert, N.A. Chernova, N. Pereira, F. Omenya, F. Badway, X. Hua, M. Ruotolo, R. Zhang, L. Wu, V. Volkov, D. Su, B. Key, M. Stanley Whittingham, C.P. Grey, G.G. Amatucci, Y. Zhu, J. Graetz, J. Am. Chem. Soc. 133 (2011) 18828–18836.
[4] L. Wang, Z. Wu, J. Zou, P. Gao, X. Niu, H. Li, L. Chen, Joule 3 (2019) 2086–2102.
[5] K. Chen, M. Lei, Z. Yao, Y. Zheng, J. Hu, C. Lai, C. Li, Sci. Adv. 7 (2021) eabj1491.
[6] J. Hu, Y. Zhang, D. Cao, C. Li, J. Mater. Chem. A 4 (2016) 16166–16174.
[7] F. Wang, S.W. Kim, D.H. Seo, K. Kang, L. Wang, D. Su, J.J. Vajo, J. Wang, J. Graetz, Nat. Commun. 6 (2015) 6668.
[8] F. Wu, J. Maier, Y. Yu, Chem. Soc. Rev. 49 (2020) 1569–1614.
[9] C. Li, K. Chen, X. Zhou, J. Maier, NPJ Comput. Mater. 4 (2018) 22.
[10] J.P. Pender, G. Jha, D.H. Youn, J.M. Ziegler, I. Andoni, E.J. Choi, A. Heller, B.S. Dunn, P.S. Weiss, R.M. Penner, C.B. Mullins, ACS Nano 14 (2020) 1243–1295.
[11] F. Wu, O. Borodin, G. Yushin, MRS Energy Sustain. 4 (2017) 9.
[12] S.H. Yu, X. Feng, N. Zhang, J. Seok, H.D. Abruña, Acc. Chem. Res. 51 (2018) 273–281.
[13] K. Wei, Y. Zhao, K. Chen, K. Sun, T. Wu, Z. Dong, Y. Cui, C. Zeng, C. Li, Adv. Funct. Mater. 31 (2021) 2009133.
[14] Q. Huang, T.P. Pollard, X. Ren, D. Kim, A. Magasinski, O. Borodin, G. Yushin, Small 15 (2019) 1804670.
[15] S.W. Kim, K.W. Nam, D.H. Seo, J. Hong, H. Kim, H. Gwon, K. Kang, Nano Today 7 (2012) 168–173.
[16] X. Fan, E. Hu, X. Ji, Y. Zhu, F. Han, S. Hwang, J. Liu, S. Bak, Z. Ma, T. Gao, S.C. Liou, J. Bai, X.Q. Yang, Y. Mo, K. Xu, D. Su, C. Wang, Nat. Commun. 9 (2018) 2324.
[17] Y. Zhao, K. Wei, H. Wu, S. Ma, J. Li, Y. Cui, Z. Dong, Y. Cui, C. Li, ACS Nano 13 (2019) 2490–2500.
[18] D. Gordon, Q. Huang, A. Magasinski, A. Ramanujapuram, N. Bensalah, G. Yushin, Adv. Energy Mater. 8 (2018) 1800213.
[19] C. Villa, S. Kim, Y. Lu, V.P. Dravid, J. Wu, ACS Appl. Mater. Interfaces 11 (2019) 647–654.
[20] Z. Lun, B. Ouyang, D.H. Kwon, Y. Ha, E.E. Foley, T.Y. Huang, Z. Cai, H. Kim, M. Balasubramanian, Y. Sun, J. Huang, Y. Tian, H. Kim, B.D. McCloskey, W. Yang, R. J. Clément, H. Ji, G. Ceder, Nat. Mater. 20 (2021) 214–221.
[21] C. Zhao, F. Ding, Y. Lu, L. Chen, Y.S. Hu, Angew. Chem. Int. Ed. 59 (2020) 264–269.
[22] T. Wang, H. Chen, Z. Yang, J. Liang, S. Dai, J. Am. Chem. Soc. 142 (2020) 4550–4554.
[23] B.S. Murty, J.W. Yeh, S. Ranganathan, P.P. Bhattacharjee, High-Entropy Alloys, 2nd ed., Elsevier Science, Amsterdam, The Netherlands, 2019.
[24] A. Sarkar, Q. Wang, A. Schiele, M.R. Chellali, S.S. Bhattacharya, D. Wang, T. Brezesinski, H. Hahn, L. Velasco, B. Breitung, Adv. Mater. 31 (2019) 1806236.
[25] Y. Sharma, B.L. Musico, X. Gao, C. Hua, A.F. May, A. Herklotz, A. Rastogi, D. Mandrus, J. Yan, H.N. Lee, M.F. Chisholm, V. Keppens, T.Z. Ward, Phys. Rev. Mater. 2 (2018) 060404.
[26] D. Bérardan, S. Franger, D. Dragoe, A.K. Meena, N. Dragoe, Phys. Status Solidi RRL 10 (2016) 328–333.
[27] J. Gild, M. Samiee, J.L. Braun, T. Harrington, H. Vega, P.E. Hopkins, K. Vecchio, J. Luo, J. Eur. Ceram. Soc. 38 (2018) 3578–3584.
[28] E. Castle, T. Csanádi, S. Grasso, J. Dusza, M. Reece, Sci. Rep. 8 (2018) 8609.
[29] M. Qin, Q. Yan, Y. Liu, J. Luo, J. Adv. Ceram. 10 (2021) 166–172.
[30] T. Jin, X. Sang, R.R. Unocic, R.T. Kinch, X. Liu, J. Hu, H. Liu, S. Dai, Adv. Mater. 30 (2018) 1707512.
[31] C.W. Tsai, S.W. Lai, K.H. Cheng, M.H. Tsai, A. Davison, C.H. Tsau, J.W. Yeh, Thin Solid Films 520 (2012) 2613–2618.
[32] R.Z. Zhang, F. Gucci, H. Zhu, K. Chen, M.J. Reece, Inorg. Chem. 57 (2018) 13027–13033.
[33] Q. Wang, A. Sarkar, D. Wang, L. Velasco, R. Azmi, S.S. Bhattacharya, T. Bergfeldt, A. Düvel, P. Heitjans, T. Brezesinski, H. Hahn, B. Breitung, Energy Environ. Sci. 12 (2019) 2433–2442.
[34] C.M. Rost, E. Sachet, T. Borman, A. Moballegh, E.C. Dickey, D. Hou, J.L. Jones, S. Curtarolo, J.P. Maria, Nat. Commun. 6 (2015) 8485.
[35] A. Sarkar, L. Velasco, D. Wang, Q. Wang, G. Talasila, L. de Biasi, C. Kübel, T. Brezesinski, S.S. Bhattacharya, H. Hahn, B. Breitung, Nat. Commun. 9 (2018) 3400.
[36] E. Lökçü, Ç. Toparli, M. Anik, ACS Appl. Mater. Interfaces 12 (2020) 23860–23866.
[37] P.A. Sukkurji, Y. Cui, S. Lee, K. Wang, R. Azmi, A. Sarkar, S. Indris, S.S. Bhattacharya, R. Kruk, H. Hahn, Q. Wang, M. Botros, B. Breitung, J. Mater. Chem. A 9 (2021) 8998–9009.
[38] H. Shinotsuka, S. Tanuma, C.J. Powell, D.R. Penn, Surf. Interface Anal. 47 (2015) 871–888.
[39] P. Giannozzi, S. Baroni, N. Bonini, M. Calandra, R. Car, C. Cavazzoni, D. Ceresoli, G.L. Chiarotti, M. Cococcioni, I. Dabo, A. Dal Corso, S. De Gironcoli, S. Fabris, G. Fratesi, R. Gebauer, U. Gerstmann, C. Gougoussis, A. Kokalj, M. Lazzeri, L. Martin-Samos, N. Marzari, F. Mauri, R. Mazzarello, S. Paolini, A. Pasquarello, L. Paulatto, C. Sbraccia, S. Scandolo, G. Sclauzero, A.P. Seitsonen, A. Smogunov, P. Umari, R.M. Wentzcovitch, J. Phys. Condens. Matter 21 (2009) 395502.
[40] J.H. Scofield, J. Electron Spectros. Relat. Phenomena 8 (1976) 129–137.
[41] J.M. Smith, S.P. Jones, L.D. White, Gastroenterology 72 (1977) 193.
[42] J.P. Perdew, A. Ruzsinszky, G.I. Csonka, O.A. Vydrov, G.E. Scuseria, L.A. Constantin, X. Zhou, K. Burke, Phys. Rev. Lett. 100 (2008) 136406.
[43] M. Cococcioni, S. De Gironcoli, Phys. Rev. B 71 (2005) 035105.
[44] N. Scott Weingarten, E.F.C. Byrd, Comput. Mater. Sci. 96 (2015) 312–318.
[45] A. Urban, I. Matts, A. Abdellahi, G. Ceder, Adv. Energy Mater. 6 (2016) 1600488.
[46] A. Van De Walle, P. Tiwary, M. De Jong, D.L. Olmsted, M. Asta, A. Dick, D. Shin, Y. Wang, L.Q. Chen, Z.K. Liu, Calphad Comput. Coupling Phase Diagrams Thermochem. 42 (2013) 13–18.
[47] N. Pereira, F. Badway, M. Wartelsky, S. Gunn, G.G. Amatucci, J. Electrochem. Soc. 156 (2009) A407.
[48] L.Y. Kuo, O. Guillon, P. Kaghazchi, J. Mater. Chem. A 8 (2020) 13832–13841.
[49] L.Y. Kuo, O. Guillon, P. Kaghazchi, ACS Sustain. Chem. Eng. 9 (2021) 7437–7446.
[50] I. Hwang, S.K. Jung, E.S. Jeong, H. Kim, S.P. Cho, K. Ku, H. Kim, W.S. Yoon, K. Kang, Nano Res. 10 (2017) 4388–4397.
[51] D. Dees, E. Gunen, D. Abraham, A. Jansen, J. Prakash, J. Electrochem. Soc. 152 (2005) A1409.
[52] J. Hwang, K. Matsumoto, R. Hagiwara, J. Phys. Chem. C 122 (2018) 26857–26864.
[53] R. Tatara, P. Karayaylali, Y. Yu, Y. Zhang, L. Giordano, F. Maglia, R. Jung, J.P. Schmidt, I. Lund, Y. Shaohorn, J. Electrochem. Soc. 166 (2019) A5090–A5098.
[54] Y.S. Chen, J.F. Kang, B. Chen, B. Gao, L.F. Liu, X.Y. Liu, Y.Y. Wang, L. Wu, H.Y. Yu, J.Y. Wang, Q. Chen, E.G. Wang, J. Phys. D. Appl. Phys. 45 (2012) 065303.
[55] M. Chhetri, S. Sultan, C.N.R. Rao, Proc. Natl. Acad. Sci. U. S. A. 114 (2017) 8986–8990.
[56] C.J. Jenks, S.L. Chang, J.W. Anderegg, P.A. Thiel, D.W. Lynch, Phys. Rev. B 54 (1996) 6301–6306.
[57] K. Rui, Z. Wen, Y. Lu, J. Jin, C. Shen, Adv. Energy Mater. 5 (2015) 1401716.
[58] Y. Huang, R. Ding, D. Ying, W. Shi, Y. Huang, C. Tan, X. Sun, P. Gao, E. Liu, Nanoscale Adv. 1 (2019) 4669–4678.
[59] Z. Fu, C. Li, W. Liu, J. Ma, Y. Wang, Q. Qin, J. Electrochem. Soc. 152 (2005) E50.
[60] N. Yamakawa, M. Jiang, B. Key, C.P. Grey, J. Am. Chem. Soc. 131 (2009) 10525–10536.
[61] X. Hua, A.S. Eggeman, E. Castillo-Martínez, R. Robert, H.S. Geddes, Z. Lu, C.J. Pickard, W. Meng, K.M. Wiaderek, N. Pereira, G.G. Amatucci, P.A. Midgley, K.W. Chapman, U. Steiner, A.L. Goodwin, C.P. Grey, Nat. Mater. 20 (2021) 841–850.
[62] A.W. Xiao, H.J. Lee, I. Capone, A. Robertson, T.U. Wi, J. Fawdon, S. Wheeler, H.W. Lee, N. Grobert, M. Pasta, Nat. Mater. 19 (2020) 644–654.
[63] P. Poizot, S. Laruelle, S. Grugeon, L. Dupont, J. Tarascon, Nature 407 (2000) 496–499.